

ADAPTIVE NEURAL NETWORK-BASED UNSCENTED KALMAN FILTER FOR SPACECRAFT POSE TRACKING AT RENDEZVOUS

Tae Ha Park* and Simone D’Amico[†]

This paper presents a neural network-based Unscented Kalman Filter (UKF) to track the pose (i.e., position and orientation) of a known, noncooperative, tumbling target spacecraft in a close-proximity rendezvous scenario. The UKF estimates the relative orbital and attitude states of the target with respect to the servicer based on the pose information extracted from incoming monocular images of the target spacecraft with a Convolutional Neural Network (CNN). In order to enable reliable tracking, the process noise covariance matrix of the UKF is tuned online using adaptive state noise compensation. Specifically, the closed-form process noise model for the relative attitude dynamics is newly derived and implemented. In order to enable a comprehensive analysis of the performance and robustness of the proposed CNN-powered UKF, this paper also introduces the Satellite Hardware-In-the-loop Rendezvous Trajectories (SHIRT) dataset which comprises the labeled imagery of two representative rendezvous trajectories in low Earth orbit. For each trajectory, two sets of images are respectively created from a graphics renderer and a robotic testbed to allow testing the filter’s robustness across domain gap. The proposed UKF is evaluated on both domains of the trajectories in SHIRT and is shown to have sub-decimeter-level position and degree-level orientation errors at steady-state.

INTRODUCTION

The on-board estimation and tracking of the pose (i.e., position and orientation) of a target Resident Space Object (RSO) is a key-enabling technology for various on-orbit servicing¹ and active debris removal² missions. In these missions, real-time information of the target’s pose with respect to the servicer spacecraft is required to plan and execute safe, autonomous and fuel-efficient rendezvous and docking trajectories. Extracting pose from a single or a sequence of images captured with a low Size-Weight-Power-Cost (SWaP-C) sensor such as a monocular camera is especially attractive in comparison to more complex sensor systems such as Light Detection and Ranging (LiDAR) or stereovision. This paper considers the case of monocular pose tracking of a single known, noncooperative, possibly tumbling target satellite, which is representative of a servicing mission.

Recent approaches to spacecraft pose estimation from monocular images rely on Machine Learning (ML) and Convolutional Neural Networks (CNN) to learn the implicit mapping between an image and the pose information.³⁻⁸ In spaceborne applications, acquiring a large number of labeled images of the specific target RSO from different space operational environments is prohibitively expensive. Therefore, the available datasets for training spaceborne ML models depend almost exclusively on computer graphics engines to render synthetic images at large scale. The examples include OpenGL for the images of the Tango spacecraft from the PRISMA mission⁹ in the SPEED dataset,^{3,10,11} Blender for those of the Envisat spacecraft by Pasqualetto Cassinis et al.^{5,12} and the Cygnus spacecraft by Black et al.,⁶ and Unreal Engine for Soyuz in the URSO dataset.⁸ However, as evidenced by the result of the first Satellite Pose Estimation Competition (SPEC2019),¹⁰ the models trained exclusively on synthetic images suffer from domain gap,^{13,14} i.e., its performance on different image domains with dissimilar data distributions (e.g., spaceborne images) degrades severely as it overfits to the features specific to the synthetic imagery.

*PhD Candidate, Department of Aeronautics & Astronautics, Stanford University, Stanford CA 94305.

[†]Associate Professor, Department of Aeronautics & Astronautics, Stanford University, Stanford CA 94305.

Recently, the advent of the SPEED+ dataset made it possible to comprehensively analyze a CNN’s robustness against domain gap.^{15,16} In addition to 60,000 synthetic images, SPEED+ also includes nearly 10,000 images of the Tango mockup model captured from the robotic Testbed for Rendezvous and Optical Navigation (TRON) facility at Stanford’s Space Rendezvous Laboratory (SLAB). These Hardware-In-the-Loop (HIL) images are captured with high-accuracy pose labels from a high-fidelity space simulation environment equipped with calibrated light boxes and a metal halide sun lamp that respectively simulate diffuse and direct light typically encountered in the Earth orbits. The SPEED+ dataset was used for the second Satellite Pose Estimation Competition (SPEC2021)* with emphasis on bridging the domain gap between the synthetic training and HIL test images. Specifically, the pose labels of the HIL images are kept private, so the participants were forced to design a robust pose estimation algorithm with only the labeled synthetic images and optionally the unlabeled HIL images as one would for an actual space mission.

In response to the challenge posed by SPEED+, Park and D’Amico recently proposed Spacecraft Pose Network v2 (SPNv2)¹⁷ to bridge the domain gap in SPEED+ via a multi-task learning architecture and extensive data augmentation. As visualized in Figure 1, SPNv2 consists of a shared, multi-scale feature encoder followed by multiple prediction heads that perform different yet related tasks such as bounding box prediction, pose regression, heatmap prediction around surface keypoints defined in advance, and satellite foreground segmentation. The authors demonstrate that SPNv2, which is trained exclusively on synthetic images, generalizes better to unseen HIL images when jointly trained on different tasks with exclusive data augmentation, such as random solar flare and style augmentation.¹⁸ Furthermore, the shared feature encoder of SPNv2 can be refined on unlabeled HIL images via Online Domain Refinement (ODR), which modulates the parameters associated with the normalization layers of SPNv2 such as Batch Normalization (BN).¹⁹ Specifically, the normalization layer parameters constitute less than 1% of all learnable weights of the feature encoder, so ODR allows for an efficient tuning of SPNv2 via self-supervised learning to further improve its predictions on the HIL images that it has not observed during the offline training phase.

The capability of SPNv2 has only been showcased on single-image basis. In fact, only a few approaches extend the application of CNN beyond single images to trajectories and video streams. Some examples include Proença and Gao⁸ who qualitatively test their CNN on a video of the Soyuz spacecraft captured in LEO and Pasqualetto Cassinis et al.¹² who test their CNN on 100 images of the Envisat mockup spacecraft captured at the Orbital Robotics and GNC lab of ESTEC. On the other hand, Pasqualetto et al.⁵ integrate a CNN into an Extended Kalman Filter (EKF), but it is only tested on a trajectory of synthetic images. To the authors’ best knowledge, there is currently no literature that simultaneously achieves (1) integration of CNN or any ML models into a navigation filter for space missions and (2) evaluation of its performance and robustness on spacecraft trajectory images that originate from a source different from the synthetic training images. Therefore, the goal of this paper is to accomplish the two aforementioned challenges.

The primary contribution of this paper is the integration of SPNv2 into an Unscented Kalman Filter (UKF)²⁰ to enable continuous, stable pose tracking of a noncooperative spacecraft from a sequence of images during a rendezvous phase. The proposed UKF tracks the pose of the target spacecraft relative to the servicer, which consists of 6D orbital state, orientation, and angular velocity. Specifically, in order to reliably track the relative orientation in the Kalman filter framework, the technique from the Multiplicative Extended Kalman Filter (MEKF)^{21,22} and Unscented Quaternion Estimator (USQUE)²³ is adopted in which the UKF state vector tracks the Modified Rodrigues Parameter (MRP)²⁴ associated with the error-quaternion of the relative orientation between subsequent time updates. To further stabilize the filter convergence amidst time-varying noise due to the target’s tumbling and noisy measurements provided by SPNv2, the process noise covariance matrix (Q) is adjusted at each iteration using the Adaptive State Noise Compensation (ASNC)²⁵ which solves for an optimal positive semi-definite matrix Q based on the estimates from the Covariance Matching (CM)²⁶ and the underlying continuous-time dynamics. Specifically, in addition to the process noise covariance matrix model derived for various orbital states by Stacey & D’Amico,²⁷ an analytical model for the process noise of the attitude dynamics is newly derived and implemented.

The secondary contribution of this paper is the Satellite Hardware-In-the-loop Rendezvous Trajectories

*<https://kelvins.esa.int/pose-estimation-2021/>

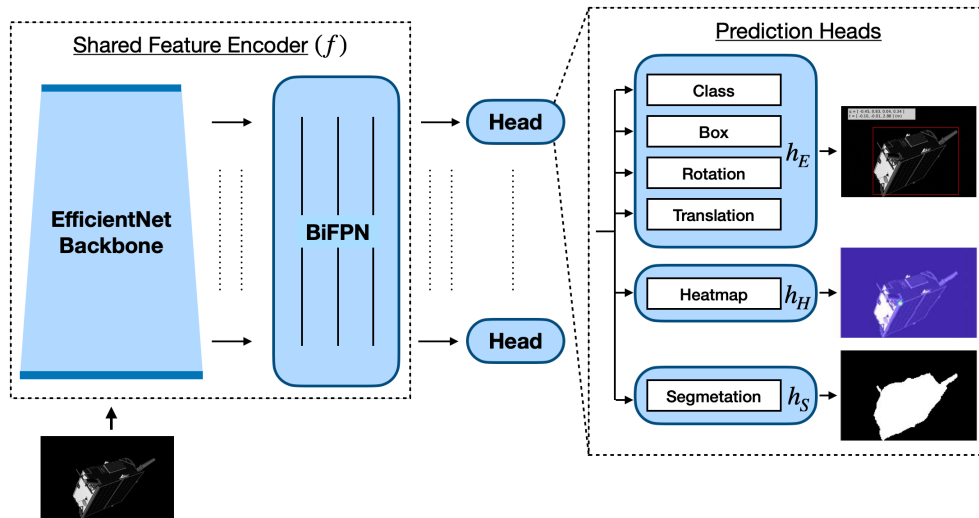


Figure 1: The overall architecture of SPNv2. Figure from Park and D’Amico.¹⁷

(SHIRT) dataset. The SHIRT dataset consists of two rendezvous trajectory scenarios (ROE1 and ROE2) in Low Earth Orbit (LEO) from two different image sources. One is the OpenGL-based computer graphics renderer used to synthesize the `synthetic` dataset of SPEED+, and the other is the TRON facility illuminated with the Earth albedo light boxes used to create the `lightbox` domain imagery of SPEED+. In ROE1, the servicer maintains the along-track separation typical of a standard v-bar hold point while the target spins about one axis, whereas in ROE2, the servicer slowly approaches the target tumbling about two axes. The SHIRT dataset is employed to evaluate the performance of SPNv2-integrated UKF across the image domain gap. It is shown that the UKF with ASNC and SPNv2 trained on the SPEED+ `synthetic` training set is able to achieve a sub-decimeter-level position and a degree-level orientation error at steady-state on `lightbox` images which SPNv2 has not seen during its training phase. To the best of the authors’ knowledge, this is the first time a CNN’s performance across domain gap is systematically tested on spacecraft trajectory images whilst integrated into a navigation filter. The SHIRT dataset will be made publicly available with all relevant metadata in the future.

This paper first begins with a brief overview of SPNv2 then describes the UKF design, including dynamics and measurement models, time and measurement updates, and closed-form expressions for the ASNC models. Afterwards, the characteristics and generation process of the SHIRT dataset is explained, followed by the experiments and results.

OVERVIEW OF SPNV2

In this work, SPNv2¹⁷ is used as the image processor. As shown in Figure 1, SPNv2 is a multi-scale, multi-task learning CNN with a shared feature encoder followed by multiple prediction heads. Namely, the EfficientPose head (h_E) follows the implementation of EfficientPose²⁸ to predict the bounding box around the spacecraft and directly regress the translation and orientation vectors of the target. The Heatmap head (h_H) outputs K heatmaps of size $H \times W$ whose peaks are associated with the 2D projected locations of K pre-designated keypoints of the target spacecraft. Finally, the Segmentation head (h_S) performs binary pixel-wise classification of the spacecraft foreground. All prediction heads of SPNv2 are jointly trained on the SPEED+ `synthetic` training set during the offline training phase.

Given the unique multi-task learning structure of SPNv2, the pose predictions can be retrieved from the outputs of either h_E or h_H . Specifically, given the known 3D coordinates of K keypoints in the target model’s reference frame, the corresponding 2D keypoint locations can be extracted from the peaks of heatmaps from h_H , which are then converted to 6D pose by solving Perspective- n -Point (PnP)²⁹ along with their 3D counterparts.

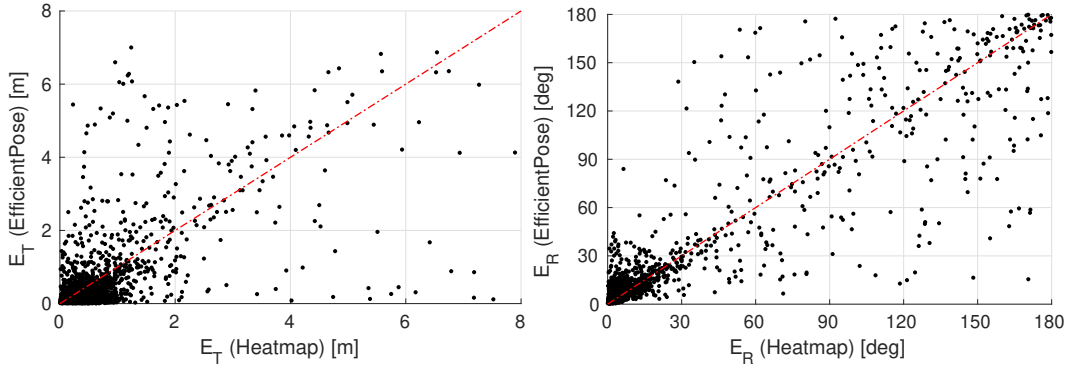


Figure 2: The comparison of E_T and E_R for translation and rotation predicted from h_H and h_E , respectively. The red line indicates an identity function.

For example, Figure 2 compares the translation error (E_T) and rotation error (E_R) of the outputs from h_H via EPnP³⁰ and h_E , respectively, by SPNv2 on the SPEED+ lightbox test set. The metrics are defined as

$$E_T = \|\hat{\mathbf{t}} - \mathbf{t}\|, \quad E_R = \arccos \frac{\text{tr}(\mathbf{R}\hat{\mathbf{R}}^\top) - 1}{2} \quad (1)$$

where (\mathbf{R}, \mathbf{t}) and $(\hat{\mathbf{R}}, \hat{\mathbf{t}})$ are respectively the predicted and ground-truth rotation matrices and translation vectors. Then, It is evident from Figure 2 that for most samples, predictions made from one head is often better than the other with weak correlation. Therefore, the redundant pose information from SPNv2 can be used to hedge against the failure of one prediction head with another.

In this work, measurements from both h_E and h_H are provided to the navigation filter. In addition to the offline robust training on `synthetic` images, Online Domain Refinement (ODR) can also be performed on the incoming target domain `unlabeled` images (e.g., SPEED+ lightbox and sunlamp test domains) by tuning the parameters of the normalization layers of the SPNv2’s feature encoder via self-supervised entropy minimization on the foreground segmentation task (h_S). While ODR has shown to further refine the performance of SPNv2 by couple centimeters and degrees,¹⁷ it is not considered in this paper as it is shown that the UKF with ASNC can achieve remarkable performance without requiring an additional refinement procedure (see Experiments section).

In this work, the batch-agnostic variant of the SPNv2 architecture is used, which has about 52.5M learnable parameters in the feature encoder and built with Group Normalization (GN) layers³¹ throughout the network. Note that the computational efficiency of a neural network is not the main focus of this paper and will be studied in the future. For more information on SPNv2 and its characteristics, the readers are referred to Park and D’Amico.¹⁷

UNSCENTED KALMAN FILTER DESIGN

In this work, the SPNv2 pre-trained on the SPEED+ `synthetic` training set is fused with a UKF to track the position and orientation of a known, noncooperative, potentially tumbling target spacecraft with respect to the servicer. In order to reliably estimate and update the target’s orientation, the techniques from the Multiplicative Extended Kalman Filter (MEKF)^{21,22,32} and Unscented Quaternion Estimator (USQUE)²³ are adopted in which the UKF state vector tracks the Modified Rodrigues Parameter (MRP)²⁴ associated with the error-quaternion of the relative orientation state between subsequent time updates. Specifically, the UKF state vector describes the relative state of the target (T) with respect to the servicer (S) and is given as

$$\mathbf{x} = [\delta\boldsymbol{\alpha}^\top \quad \delta\mathbf{p}^\top \quad (\mathbf{w}_{S/T}^T)^\top]^\top, \quad (2)$$

where $\delta\boldsymbol{\alpha} \in \mathbb{R}^6$ is the osculating Relative Orbital Elements (ROE) representing the 6D state of the target relative to the servicer, $\delta\mathbf{p} \in \mathbb{R}^3$ denotes a MRP vector representing the local error-quaternion, and $\mathbf{w}_{S/T}^T \in \mathbb{R}^3$

describes the relative angular velocity of the servicer with respect to the target expressed in the target's principal axes. In this work, a set of nonsingular ROE³³ is used; however, any representation could be used depending on the orbit regime under consideration. Specifically, given the set of equinoctial elements,

$$\boldsymbol{\alpha} = \begin{bmatrix} a \\ e_x \\ e_y \\ i_x \\ i_y \\ \lambda \end{bmatrix} = \begin{bmatrix} a \\ e \cos(\Omega + \omega) \\ e \sin(\Omega + \omega) \\ \tan\left(\frac{i}{2}\right) \cos \Omega \\ \tan\left(\frac{i}{2}\right) \sin \Omega \\ \Omega + \omega + M \end{bmatrix} \quad (3)$$

where $[a, e, i, \Omega, \omega, M]$ are classical Keplerian orbital elements, the set of nonsingular ROE is defined as

$$\delta\boldsymbol{\alpha} = \begin{bmatrix} \delta a \\ \delta\lambda \\ \delta e_x \\ \delta e_y \\ \delta i_x \\ \delta i_y \end{bmatrix} = \begin{bmatrix} (a_T - a_S)/a_S \\ \lambda_T - \lambda_S \\ e_{x,T} - e_{x,S} \\ e_{y,T} - e_{y,S} \\ i_{x,T} - i_{x,S} \\ i_{y,T} - i_{y,S} \end{bmatrix}. \quad (4)$$

The 3D MRP vector is related to a 4D error-quaternion vector $\delta\mathbf{q} = [\delta q_w \ \delta\mathbf{q}_v^\top]^\top$ via

$$\delta\mathbf{p} = \frac{4}{1 + \delta q_w} \delta\mathbf{q}_v, \quad (5)$$

which has been used successfully in literature for spacecraft attitude estimation.^{21,22} With this parametrization, $\|\delta\mathbf{p}\|$ is equal to the Euler angles for small errors.²³

In UKF with N state variables, $2N + 1$ sigma points are generated and propagated over the measurement interval. Then, the propagated sigma points are averaged to compute the mean state and the state covariance matrix. The same procedure repeats for each sigma point during the measurement update as well. In USQUE, a separate quaternion state vector is kept to track the rotating motion of the target. The MRP vector is set to a zero prior to generating sigma points at each time step; then, the error-quaternions are propagated during the time update, which are then converted back to MRP to compute the mean state. The mean MRP is converted back to the mean error-quaternion, which is multiplied to the current quaternion state to update the target's attitude estimation. For more details on the algorithmic implementation of USQUE, the readers are referred to Crassidis and Markley.²³

Time Update

The time update of UKF at k -th step propagates the sigma point of the state vector over the propagation interval $\Delta t_k = t_k - t_{k-1}$. The advantage of UKF is that the nonlinear dynamics and measurement models can be retained throughout the updates. However, in this work, a closed-form State Transition Matrix (STM) derived by Koenig et al.³³ under the small interspacecraft separation assumption is used for the ROE update due to its simplicity. Specifically, the J2-perturbed STM for nonsingular ROE is used, so that

$$\delta\boldsymbol{\alpha}_{k|k-1} = \boldsymbol{\Phi}_{\text{NS},k}^{\text{J}_2}(\boldsymbol{\alpha}_S(t_k), \Delta t_k) \delta\boldsymbol{\alpha}_{k-1|k-1}, \quad (6)$$

where $\boldsymbol{\Phi}_{\text{NS},k}^{\text{J}_2}$ is the STM that is a function of the servicer's Orbital Elements (OE) at t_k and the propagation interval Δt_k . Note that while a well-defined STM is used for the time update of the ROE state in this work, the UKF framework permits more complex and nonlinear dynamics update procedures for any other relative orbital state representations.

For orientation, the quaternion state vector, $\mathbf{q}_{T/S}$, tracks the orientation of the target relative to the servicer. The quaternion dynamics is given as

$$\dot{\mathbf{q}}_{T/S,k} = \frac{1}{2} \boldsymbol{\Omega}(\mathbf{w}_{T/S,k}^T) \otimes \mathbf{q}_{T/S,k}, \quad \text{where } \boldsymbol{\Omega}(\mathbf{w}) = \begin{bmatrix} 0 & -\mathbf{w}^\top \\ \mathbf{w} & -[\mathbf{w}]_\times \end{bmatrix}, \quad (7)$$

$[\mathbf{w}]_{\times}$ is the skew-symmetric cross product matrix of \mathbf{w} , and \otimes denotes the quaternion multiplication. The expression for relative angular acceleration is derived as³⁴

$$\dot{\mathbf{w}}_{S/T,k}^T = \mathbf{R}_{T/S,k} [\mathbf{I}_S^{-1} (\mathbf{m}_{S,k} - \mathbf{w}_{S,k}^S \times \mathbf{I}_S \mathbf{w}_{S,k}^S)] - \mathbf{I}_T^{-1} (\mathbf{m}_{T,k} - \mathbf{w}_{T,k}^T \times \mathbf{I}_T \mathbf{w}_{T,k}^T) - \mathbf{w}_{T,k}^T \times \mathbf{w}_{S/T,k}^T, \quad (8)$$

where $\mathbf{I}_S, \mathbf{I}_T \in \mathbb{R}^{3 \times 3}$ are respectively the servicer's and the target's principal moment of inertia matrices, and $\mathbf{m}_S, \mathbf{m}_T \in \mathbb{R}^3$ are respectively the control moments about the servicer's and the target's principal axes. The target's absolute angular velocity can be computed from the current estimates as $\mathbf{w}_{T,k}^T = \mathbf{R}_{T/S,k} \mathbf{w}_{S,k}^S - \mathbf{w}_{S/T,k}^T$, where $\mathbf{R}_{T/S,k}$ is the direction cosine matrix corresponding to the orientation described by $\mathbf{q}_{T/S,k}$. In this work, the target's inertia matrix are assumed known with high accuracy, and $\mathbf{m}_T = \mathbf{0}_{3 \times 1}$ is assumed for a non-operating target spacecraft or debris. In order to accurately update the quaternion and relative angular velocity considering the length of the update interval and the rate at which the target could tumble, Equations 7 and 8 are integrated via fourth-order Runge Kutta.

Measurement Update

SPNV2 consists of a shared feature encoder and two prediction heads that extract two sets of pose-related measurements from a single image. First, the Heatmap head (h_H) provides 2D heatmaps associated with the projected location of K pre-designated keypoints on the surface of the target spacecraft. The exact locations of the projected keypoints correspond to the peaks of the heatmaps. Second, the EfficientPose head (h_E) directly outputs the predicted position (\mathbf{t}_E) and orientation (\mathbf{q}_E) of the target with respect to the camera. Inspired by USQUE,²³ the quaternion measurement is represented as the MRP vector corresponding to the error-quaternion between the measured and currently estimated orientation after time update, i.e.,

$$\delta \mathbf{q}_{E,k} = \mathbf{q}_{E,k} \otimes \mathbf{q}_{T/S,k|k-1}^{-1}, \quad (9)$$

which is converted to $\delta \mathbf{p}_{E,k}$ via Eq. 5. Then, the complete measurement vector, $\mathbf{y} \in \mathbb{R}^{2K+6}$, is given as

$$\mathbf{y}_k = [x_{1,k} \ y_{1,k} \ \dots \ x_{K,k} \ y_{K,k} \ \mathbf{t}_{E,k}^T \ \delta \mathbf{p}_{E,k}^T]^T. \quad (10)$$

At each step, the expected measurements for the keypoints can be computed via projective transformation for a pinhole camera model. Given the camera intrinsic matrix $\mathbf{K} \in \mathbb{R}^{3 \times 3}$, the pose of the camera (C) with respect to the servicer spacecraft's principal frame ($\mathbf{r}_{C/S}^S, \mathbf{q}_{C/S}$), and the known 3D coordinates of the keypoints in the target's principal frame $\mathbf{k}_j^T \in \mathbb{R}^3, j = 1, \dots, K$, the expected keypoint location on the image is given as

$$s \begin{bmatrix} \hat{x}_j^k \\ \hat{y}_j^k \\ 1 \end{bmatrix} = \mathbf{K} [\mathbf{R}_{C/T,k} \mid \mathbf{r}_{T/C,k}^C] \begin{bmatrix} \mathbf{k}_j^T \\ 1 \end{bmatrix}. \quad (11)$$

Here, s is an arbitrary scaling factor, and

$$\mathbf{R}_{C/T,k} = \mathbf{R}_{C/S} \mathbf{R}_{S/T,k}, \quad (12)$$

$$\mathbf{r}_{T/C,k}^C = \mathbf{R}_{C/S} \mathbf{r}_{T/S,k}^S + \mathbf{r}_{S/C}^C, \quad (13)$$

where $\mathbf{R}_{C/S}$ is the orientation of the camera frame with respect to the servicer's principal axes frame, and $\mathbf{r}_{S/C}^C$ denotes the translation of the servicer's center of mass relative to the camera expressed in the camera frame. Both quantities are assumed known from the servicer's model and remain constant throughout the mission. Lastly, the expected translation vector can be converted from the nonsingular ROE state $\delta \boldsymbol{\alpha}$, and the expected MRP vector is obtained via Eq. 9.

Noting that the spread of the heatmap about its peak can be interpreted as a confidence associated with the prediction of the keypoint location, the covariance matrix of the (x, y) -coordinates of a keypoint, $\mathbf{C} \in \mathbb{R}^{2 \times 2}$, can be computed as⁵

$$\mathbf{C} = \begin{bmatrix} \text{cov}(x, x) & \text{cov}(x, y) \\ \text{cov}(y, x) & \text{cov}(y, y) \end{bmatrix}, \quad \text{where } \text{cov}(x, y) = \sum_{i=1}^P w_i (x_i - p_x)(y_i - p_y). \quad (14)$$

Here, (p_x, p_y) denotes the coordinates of the peak, w_i is the normalized intensity of the i -th pixel, and P is the number of pixels in the image. Then, these covariance matrices for each keypoint is used to construct the corresponding portion of the measurement noise matrix, $\mathbf{R} \in \mathbb{R}^{(2K+6) \times (2K+6)}$, at each iteration by populating the 2×2 entries along the diagonal of the upper-left $2K \times 2K$ portion of \mathbf{R} with the corresponding covariance matrices. For more details, the readers are referred to Pasqualetto Cassinis et al.⁵

The measurement noise covariance for the h_E measurements cannot be estimated online on an unknown image domain as it is done for the keypoints. Therefore, the lower-right 6×6 portion of \mathbf{R} derives from the SPNv2's performance on the `synthetic` validation set of SPEED+ scaled by some arbitrary ad hoc constants. The cross-correlation between the keypoint and vector measurements are not considered, as Figure 2 indicates that the pose outputs from h_H and h_E are weakly correlated.

Outlier Rejection

In order to mitigate an unexpected failure of SPNv2 on the test domain images that it has not seen during the offline training phase, any outlier measurements are detected and discarded based on the squared Mahalanobis distance of the UKF innovation,²¹ defined as

$$d_k^2 = \Delta_k^y \mathbf{S}_k^{-1} \Delta_k^y \quad (15)$$

Here, $\Delta_k^y = \mathbf{y}_k - \mathbf{h}(\mathbf{x}_{k|k-1})$ is the innovation or pre-fit residual, where $\mathbf{h}(\cdot)$ is the nonlinear measurement model, and \mathbf{S}_k is the measurement covariance matrix of UKF. The squared Mahalanobis distance is computed for each keypoint, translation and MRP vectors. Since d^2 follows the Chi-Square distribution with 2 Degrees-of-Freedom (DoF) for keypoints and 3DoF for translation and MRP vectors, if any one of them is beyond the threshold determined based on the inverse Chi-Square distribution at some specified probability p , that measurement is rejected. In this work, $p = 0.99$ is set. If all measurements are rejected, only the time update is performed.

Adaptive State Noise Compensation

The process noise covariance matrix, $\mathbf{Q} \in \mathbb{R}^{12 \times 12}$, is adaptively tuned at each time step via Adaptive State Noise Compensation (ASNC).²⁵ ASNC ensures that the tuned process noise matrix is positive semi-definite while respecting the continuous time-varying dynamics model of the system. First, the ordinary State Noise Compensation (SNC) models the process noise covariance at time step k as

$$\mathbf{Q}_k = \int_{t_{k-1}}^{t_k} \Phi(t_k, \tau) \mathbf{\Gamma}(\tau) \tilde{\mathbf{Q}}_k \mathbf{\Gamma}(\tau)^\top \Phi(t_k, \tau)^\top d\tau, \quad (16)$$

where $\Phi(t_k, t)$ is the STM which propagates the state vector from time t to t_k , $\mathbf{\Gamma}(t)$ is the process noise mapping matrix, and $\tilde{\mathbf{Q}}_k$ is the process noise power spectral density matrix. The $\tilde{\mathbf{Q}}_k$ matrix is assumed constant over the measurement interval; moreover, the process noise is assumed independent across the dimensions such that $\tilde{\mathbf{Q}}_k$ is diagonal. Then, Eq. 16 becomes linear in $\tilde{\mathbf{Q}}_k$, and the unique elements of the symmetric matrix \mathbf{Q}_k and the diagonal elements of $\tilde{\mathbf{Q}}_k$ can be related as

$$\mathbf{Q}_k^{\text{vech}} = \mathbf{X}_k \tilde{\mathbf{Q}}_k^{\text{diag}}, \quad (17)$$

where $\mathbf{A}^{\text{vech}} = \text{vech}(\mathbf{A})$ denotes the half-vectorization operation which returns a vector of the lower-triangular elements of the symmetric matrix \mathbf{A} , and $\mathbf{A}^{\text{diag}} = \text{diag}(\mathbf{A})$ returns a vector of the diagonal elements of \mathbf{A} . The linear mapping matrix \mathbf{X}_k is based on Φ and $\mathbf{\Gamma}$ that vary depending on the state representation and the underlying dynamics model. The process noise matrices for various absolute and relative orbital state representations are provided by Stacey and D'Amico²⁷ assuming that the noise manifests as unmodeled acceleration in the Radial-Tangential-Normal (RTN) frame.

In SNC, the diagonal matrix $\tilde{\mathbf{Q}}_k$ is manually tuned offline. ASNC instead solves for the optimal $\tilde{\mathbf{Q}}_k$ by matching Eq. 16 with the corresponding estimate of $\hat{\mathbf{Q}}_k$ obtained through the covariance matching over a

sliding window,²⁶ i.e.,

$$\hat{\mathbf{Q}}_k = \frac{1}{N_W} \sum_{i=k-N_W+1}^k \mathbf{P}_{i|i} - \Phi_i \mathbf{P}_{i-1|i-1} \Phi_i^\top + \Delta_i^x \Delta_i^x{}^\top \quad (18)$$

where N_W is the length of the sliding window. Here, Δ_i^x is the state correction term defined as

$$\Delta_i^x = \mathbf{K}_k \Delta_i^y, \quad (19)$$

where \mathbf{K}_k is the Kalman gain, and Δ_i^y is the measurement innovation of Eq. 15.

The optimal $\tilde{\mathbf{Q}}_k$ for Eq. 16 is the solution to the constrained weighted least-squares minimization problem,

$$\begin{aligned} \min_{\tilde{\mathbf{Q}}_{\text{diag}}} & (\mathbf{X}_k \tilde{\mathbf{Q}}_{\text{diag}} - \hat{\mathbf{Q}}_{k+1}^{\text{vech}})^\top \mathbf{W}_k^{-1} (\mathbf{X}_k \tilde{\mathbf{Q}}_{\text{diag}} - \hat{\mathbf{Q}}_{k+1}^{\text{vech}}) \\ \text{subject to} & \tilde{\mathbf{Q}}_\ell^{\text{diag}} \leq \tilde{\mathbf{Q}}_{\text{diag}} \leq \tilde{\mathbf{Q}}_u^{\text{diag}}, \end{aligned} \quad (20)$$

where \mathbf{W}_k is the theoretical covariance of $\hat{\mathbf{Q}}_{k+1}^{\text{vech}}$, and $\tilde{\mathbf{Q}}_\ell^{\text{diag}}$ and $\tilde{\mathbf{Q}}_u^{\text{diag}}$ are respectively the element-wise lower- and upper-bounds on $\tilde{\mathbf{Q}}_{\text{diag}}$ based on a coarse a priori knowledge of the dynamical environment.

In this work, the process noise covariance matrix for the state vector in Eq. 2 is obtained via ASNC at each time step. In order to facilitate the computation, the noise components between the orbital and attitude states are decoupled, i.e.,

$$\mathbf{Q}_k = \begin{bmatrix} \mathbf{Q}_{\delta\alpha,k} & \mathbf{0}_{6 \times 6} \\ \mathbf{0}_{6 \times 6} & \mathbf{Q}_{q,k} \end{bmatrix}. \quad (21)$$

The process noise power spectral density matrices for both states are assumed diagonal by considering the unmodeled relative accelerations in the servicer's RTN frame and unmodeled torque about the target's principal axes, i.e.,

$$\tilde{\mathbf{Q}}_{\delta\alpha} = \begin{bmatrix} \tilde{\mathbf{Q}}_{\delta\alpha}^r & 0 & 0 \\ 0 & \tilde{\mathbf{Q}}_{\delta\alpha}^t & 0 \\ 0 & 0 & \tilde{\mathbf{Q}}_{\delta\alpha}^n \end{bmatrix}, \quad \tilde{\mathbf{Q}}_q = \begin{bmatrix} \tilde{\mathbf{Q}}_q^x & 0 & 0 \\ 0 & \tilde{\mathbf{Q}}_q^y & 0 \\ 0 & 0 & \tilde{\mathbf{Q}}_q^z \end{bmatrix}. \quad (22)$$

The latter is reasonable since the uncertainty of the servicer's own attitude state estimate is assumed to be much smaller than that of the target. Then, taking the ROE state as an example, the process noise covariance matrix in Eq. 16 becomes

$$\mathbf{Q}_{\delta\alpha,k} = \mathbf{X}_k^r \tilde{\mathbf{Q}}_{\delta\alpha,k}^r + \mathbf{X}_k^t \tilde{\mathbf{Q}}_{\delta\alpha,k}^t + \mathbf{X}_k^n \tilde{\mathbf{Q}}_{\delta\alpha,k}^n, \quad (23)$$

where

$$\mathbf{X}_k^i = \int_{t_{k-1}}^{t_k} \bar{\mathbf{\Gamma}}_k^i(t_k, \tau) \bar{\mathbf{\Gamma}}_k^i(t_k, \tau)^\top d\tau, \quad i \in \{r, t, n\}. \quad (24)$$

Here, $\bar{\mathbf{\Gamma}}_k(t_k, t) = \Phi(t_k, t) \mathbf{\Gamma}_k(t)$, and $\bar{\mathbf{\Gamma}}_k = [\bar{\mathbf{\Gamma}}_k^r \quad \bar{\mathbf{\Gamma}}_k^t \quad \bar{\mathbf{\Gamma}}_k^n]$. Equations 23 and 24 can now be used to construct the linear mapping of Eq. 17 as

$$\mathbf{Q}_{\delta\alpha,k}^{\text{vech}} = \mathbf{X}_k \tilde{\mathbf{Q}}_{\delta\alpha,k}^{\text{diag}} = \begin{bmatrix} | & | & | \\ \text{vech}(\mathbf{X}_k^r) & \text{vech}(\mathbf{X}_k^t) & \text{vech}(\mathbf{X}_k^n) \\ | & | & | \end{bmatrix} \begin{bmatrix} \tilde{\mathbf{Q}}_{\delta\alpha,k}^r \\ \tilde{\mathbf{Q}}_{\delta\alpha,k}^t \\ \tilde{\mathbf{Q}}_{\delta\alpha,k}^n \end{bmatrix}. \quad (25)$$

A similar expression can be constructed for the attitude dynamics as well. Once \mathbf{X}_k matrices can be constructed from Eq. 25 for both ROE and attitude states, the least-squares minimization problem of Eq. 20 can be solved individually for both states using an off-the-shelf least-squares or quadratic programming solver. In this work, MATLAB's `lsqlin` command is used to solve Eq. 20 with a non-negativity constraint, i.e., $\tilde{\mathbf{Q}}_\ell^{\text{diag}} = \mathbf{0}_{3 \times 1}$ to ensure a positive semi-definite solution.

The sections below describe in detail the process noise covariance modeling for both states.

ROE State Process Noise For a nonsingular ROE representation based on the equinoctial elements, Stacey and D'Amico²⁷ derived the process noise covariance model under the assumption of two-body motions. Specifically, for a small separation between two spacecraft, the authors first derive the process noise $\mathbf{Q}_{\delta\alpha'}$ for an alternative ROE representation defined as $\delta\alpha' = \alpha_T - \alpha_S$. Then, the process noise for nonsingular ROE can be recovered via

$$\mathbf{Q}_{\delta\alpha,k} = \mathbf{J}_{\delta\alpha}(t_k)\mathbf{Q}_{\delta\alpha',k}\mathbf{J}_{\delta\alpha}(t_k)^\top, \quad (26)$$

where

$$\mathbf{J}_{\delta\alpha}(t_k) = \left. \frac{\partial\delta\alpha}{\partial\delta\alpha'} \right|_{\delta\alpha'=0} = \begin{bmatrix} \frac{1}{a_S} & \mathbf{0}_{1 \times 4} & 0 \\ 0 & \mathbf{0}_{1 \times 4} & 1 \\ \mathbf{0}_{4 \times 1} & \mathbf{I}_{4 \times 4} & \mathbf{0}_{4 \times 1} \end{bmatrix}, \quad (27)$$

and a_S is the semi-major axis of the servicer at t_k . Noting that $\mathbf{Q}_{\delta\alpha'} = \sum_{i \in \{r,t,n\}} \mathbf{X}_k^{i'} \tilde{\mathbf{Q}}_{\delta\alpha'}$, the linear mapping matrices of Eq. 25 are now given as

$$\mathbf{X}_k^i = \mathbf{J}_{\delta\alpha}(t_k)\mathbf{X}_k^{i'}\mathbf{J}_{\delta\alpha}(t_k)^\top, \quad (28)$$

where $\mathbf{X}_k^{i'}$ of Eq. 24 for $\delta\alpha'$ is derived by Stacey and D'Amico²⁷ and partially reproduced in Appendix.

Attitude State Process Noise In order to derive the process noise covariance matrix for the attitude states, STM (Φ_q) and the process noise mapping matrix (Γ_k) must first be constructed. First, the dynamics of the MRP vector is given as²¹

$$\delta\dot{\mathbf{p}} = \left(-\frac{1}{2}[\mathbf{w}_{T/S}^T]_\times + \frac{1}{8}(\mathbf{w}_{T/S}^T)^\top \delta\mathbf{p} \right) \delta\mathbf{p} + \left(1 - \frac{1}{16}\delta\mathbf{p}^\top \delta\mathbf{p} \right) \mathbf{w}_{T/S}^T, \quad (29)$$

where $[\mathbf{w}]_\times \in \mathbb{R}^{3 \times 3}$ denotes a skew-symmetric cross product matrix of \mathbf{w} , and the dynamics of relative angular velocity is given in Eq. 8. In MEKF and USQUE frameworks, the MRP vector corresponding to the error-quaternion state is reset to zero prior to each propagation step. Therefore, assuming short propagation intervals and small relative angular velocity, the MRP dynamics equation simplifies to

$$\delta\dot{\mathbf{p}} \approx -\frac{1}{2}[\mathbf{w}_{T/S}^T]_\times \delta\mathbf{p} + \mathbf{w}_{T/S}^T = \frac{1}{2}[\mathbf{w}_{S/T}^T]_\times \delta\mathbf{p} - \mathbf{w}_{S/T}^T, \quad (30)$$

where $(\mathbf{w}_{T/S}^T)^\top \delta\mathbf{p}$ and $\delta\mathbf{p}^\top \delta\mathbf{p}$ are both assumed negligible. Likewise, the relative angular velocity dynamics in Eq. 8 approximates to

$$\dot{\mathbf{w}}_{S/T}^T \approx -[\mathbf{w}_T^T]_\times \mathbf{w}_{S/T}^T - \mathbf{I}_T^{-1} \boldsymbol{\varepsilon}_T + \mathbf{R}_{T/S,k} \dot{\mathbf{w}}_S^S, \quad (31)$$

where the term $\mathbf{w}_T^T \times \mathbf{I}_T \mathbf{w}_T^T$ is assumed negligible, which is a reasonable assumption for a small spin rate and exact if the target spins about one axis. In Eq. 31, $\boldsymbol{\varepsilon}_T \in \mathbb{R}^3$ accounts for the unmodeled torque in the system expressed in the target's principal axes frame, and $\dot{\mathbf{w}}_S^S = \mathbf{R}_{T/S} \mathbf{I}_S^{-1} (\mathbf{m}_S - \mathbf{w}_S^S \times \mathbf{I}_S \mathbf{w}_S^S)$ is due to Euler's rotational equation. Now, the continuous-time dynamics can be constructed from Eqs. 30, 31,

$$\begin{bmatrix} \delta\dot{\mathbf{p}} \\ \dot{\mathbf{w}}_{S/T}^T \end{bmatrix} = \mathbf{A} \begin{bmatrix} \delta\mathbf{p} \\ \mathbf{w}_{S/T}^T \end{bmatrix} + \mathbf{\Gamma} \boldsymbol{\varepsilon}_T + \mathbf{C} = \begin{bmatrix} \frac{1}{2}[\mathbf{w}_{S/T}^T]_\times & -\mathbf{I}_{3 \times 3} \\ \mathbf{0}_{3 \times 3} & -[\mathbf{w}_T^T]_\times \end{bmatrix} \begin{bmatrix} \delta\mathbf{p} \\ \mathbf{w}_{S/T}^T \end{bmatrix} + \begin{bmatrix} \mathbf{0}_{3 \times 3} \\ -\mathbf{I}_T^{-1} \end{bmatrix} \boldsymbol{\varepsilon}_T + \begin{bmatrix} \mathbf{0}_{3 \times 1} \\ \mathbf{R}_{T/S,k} \dot{\mathbf{w}}_S^S \end{bmatrix}, \quad (32)$$

where \mathbf{A} is the plant matrix, and $\mathbf{\Gamma}$ is the process noise mapping matrix. Then, the following STM can be obtained via zero-hold integration,²¹

$$\Phi_{q,k}(t, 0) = \begin{bmatrix} e^{\frac{1}{2}[\mathbf{w}_{S/T,k}^T]_\times t} & -\int_0^t e^{\frac{1}{2}[\mathbf{w}_{S/T,k}^T]_\times \tau} d\tau \\ \mathbf{0}_{3 \times 3} & e^{-[\mathbf{w}_T^T]_\times t} \end{bmatrix}, \quad (33)$$

Table 1: Initial servicer absolute and target relative orbital states.

	Servicer Mean OE						Target Mean ROE					
	a [km]	e [-]	i [°]	Ω [°]	ω [°]	M [°]	$a\delta a$ [m]	$a\delta\lambda$ [m]	$a\delta e_x$ [m]	$a\delta e_y$ [m]	$a\delta i_x$ [m]	$a\delta i_y$ [m]
ROE1	7078.135	0.001	98.2	189.9	0	0	0	-8	0	0	0	0
ROE2							-0.250	-8.1732	0.0257	-0.1476	-0.030	0.1724

which leads to

$$\bar{\Gamma}_k(t, 0) = \Phi_{q,k}(t, 0)\Gamma_k = \begin{bmatrix} \int_0^t e^{\frac{1}{2}[\mathbf{w}_{S/T,k}^T] \times \tau} d\tau \\ -e^{-[\mathbf{w}_{T,k}^T] \times t} \end{bmatrix} \mathbf{I}_T^{-1} = \begin{bmatrix} \Lambda_1(t) \\ -\Lambda_2(t) \end{bmatrix} \mathbf{I}_T^{-1}. \quad (34)$$

In order for $\bar{\Gamma}_k$ to be used in Eq. 24 to compute the linear mapping matrix \mathbf{X}_k^i for $i \in \{x, y, z\}$, the integral of the matrix exponential must be evaluated. From the Rodrigues' formula, the exponential of a real, skew-symmetric matrix $\mathbf{A} = [\mathbf{a}]_{\times} \in \mathbb{R}^{3 \times 3}$ is given as

$$e^{\mathbf{A}} = \mathbf{I}_{3 \times 3} + \sin \theta \hat{\mathbf{A}} + (1 - \cos \theta) \hat{\mathbf{A}}^2, \quad (35)$$

where $\theta = \|\mathbf{a}\|$, and $\hat{\mathbf{A}} = \mathbf{A}/\theta$. Applying this to the integrand of the integral term in Eq. 34 yields

$$e^{\frac{1}{2}[\mathbf{w}_1] \times \tau} = \mathbf{I}_{3 \times 3} + \sin \frac{w_1 \tau}{2} [\hat{\mathbf{w}}_1]_{\times} + \left(1 - \cos \frac{w_1 \tau}{2}\right) [\hat{\mathbf{w}}_1]_{\times}^2, \quad (36)$$

where \mathbf{w}_1 is a shorthand notation for $\mathbf{w}_{S/T,k}^T$, $w_1 = \|\mathbf{w}_1\|$, and $[\hat{\mathbf{w}}_1]_{\times} = [\mathbf{w}_1]_{\times}/w_1$. Integrating over $[0, t]$, one obtains

$$\Lambda_1(t) = \int_0^t e^{\frac{1}{2}[\mathbf{w}_1] \times \tau} d\tau = \mathbf{I}_{3 \times 3} t + \frac{2}{w_1} \left(1 - \cos \frac{w_1 t}{2}\right) [\hat{\mathbf{w}}_1]_{\times} + \left(t - \frac{2}{w_1} \sin \frac{w_1 t}{2}\right) [\hat{\mathbf{w}}_1]_{\times}^2. \quad (37)$$

Likewise,

$$\Lambda_2(t) = e^{-[\mathbf{w}_{T,k}^T] \times t} = \mathbf{I}_{3 \times 3} - (\sin w_2 t) [\hat{\mathbf{w}}_2]_{\times} + (1 - \cos w_2 t) [\hat{\mathbf{w}}_2]_{\times}^2, \quad (38)$$

where \mathbf{w}_2 is a shorthand notation for $\mathbf{w}_{T,k}^T$. The \mathbf{X}_k^i matrix in Eq. 24 can now be computed as

$$\mathbf{X}_k^i = \mathbf{I}_{T,i}^{-2} \begin{bmatrix} \bar{\mathbf{A}}_i & -\bar{\mathbf{B}}_i \\ -\bar{\mathbf{B}}_i^T & \bar{\mathbf{C}}_i \end{bmatrix} \quad (39)$$

where $\mathbf{I}_{T,i}$ is the i -th diagonal element of \mathbf{I}_T , and the analytical expression for the sub-matrices $\bar{\mathbf{A}}_i, \bar{\mathbf{B}}_i, \bar{\mathbf{C}}_i \in \mathbb{R}^{3 \times 3}$ are provided in Appendix .

SATELLITE HARDWARE-IN-THE-LOOP RENDEZVOUS TRAJECTORIES (SHIRT) DATASET

Reference Trajectory Simulation

Drawing inspiration from Sharma and D'Amico²² and D'Amico,³⁵ SHIRT includes simulations of two reference trajectories which emulate typical rendezvous scenarios in LEO. The initial orbital states for the servicer's absolute and the target's relative orbital states are presented in Table 1. Specifically, ROE1 maintains an along-track separation typical of a standard v-bar hold point, whereas ROE2 introduces a small, nonzero relative semi-major axis (δa) for the servicer to slowly approach the target. The servicer's initial mean OE, which are derived from the PRISMA mission,^{9,36} indicates that the satellites are in a dawn-dusk sun-synchronous orbit.

Table 2: SHIRT simulation parameters

Simulation Parameters	
Initial epoch	2011/07/18 01:00:00
Integrator	Runge-Kutta (Dormand-Prince) ³⁷
Step size	1 s
Simulation time	2 orbits
Force Models	
Geopotential field (degree \times order)	GGM05S (120 \times 120) ³⁸
Atmospheric density	NRLMSISE-00 ³⁹
Solar radiation pressure	Cannon-ball, conical Earth shadow
Third-body gravity	Analytical Sun & Moon ⁴⁰
Relativistic effect	1st order ⁴⁰
Torque Models	
Gravity gradient	Analytical ⁴¹
Atmospheric density	NRLMSISE-00 ³⁹
Solar radiation pressure	Conical Earth shadow
Geomagnetic field (order)	IGRF-13 (10) ⁴²

Table 3: Spacecraft parameters of Mango (servicer) and Tango (target) of PRISMA mission⁹ for force and torque models evaluation.

Spacecraft Parameters	Servicer (Mango)	Target (Tango)
Force Model Evaluation		
Spacecraft mass [kg]	154.4	42.5
Cross-sectional area (drag) [m ²]	1.3	0.38
Cross-sectional area (SRP) [m ²]	2.5	0.55
Aerodynamic drag coefficient	2.5	2.25
SRP coefficient	1.32	1.2
Torque Model Evaluation		
Number of faces	10	6
Principal moment of inertia [kg·m ²]	diag(16.70, 19.44, 18.28)	diag(2.69, 3.46, 3.11)
DCM from body to principal frame	$\begin{bmatrix} 1 & 0 & 0 \\ 0 & 1 & 0 \\ 0 & 0 & 1 \end{bmatrix}$	$\begin{bmatrix} 1 & 0 & 0 \\ 0 & -0.929 & 0.369 \\ 0 & -0.369 & -0.929 \end{bmatrix}$
Magnetic dipole moment [A·m ²]	$[0, 0, 0]^T$	$[0, 0, 5.66 \times 10^{-7}]^T$

The servicer's initial attitude, which coincides with the camera's attitude, is defined with respect to the Radial-Tangential-Normal (RTN) frame. Specifically, the camera boresight (i.e., z -axis) is initially directed along the negative along-track direction ($-\hat{T}$) and its x -axis along the cross-track direction (\hat{N}). The servicer's attitude is controlled such that the camera boresight is always pointed along $-\hat{T}$. To be more specific, the servicer's angular velocity about its body axes is set to $[n \ 0 \ 0]^T$ (rad/s), where n is the satellite mean motion, and torque is applied at each time step to negate any accumulated environmental perturbation moments. The target's initial relative attitude with respect to the servicer is given in terms of quaternion as $\mathbf{q}_o = [1/\sqrt{2} \ 1/\sqrt{2} \ 0 \ 0]^T$. The target's initial angular velocity about its principal axes is set to $\boldsymbol{\omega}_0 = [1 \ 0 \ 0]^T$ (°/s) for ROE1 and $\boldsymbol{\omega}_0 = [0 \ 0.4 \ -0.6]^T$ (°/s) for ROE2, which are reasonable for a tumbling, non-cooperative object in space.

The orbital states of respective spacecraft are numerically propagated with 1 second time step for two full orbits using the SLAB's Satellite Software (S^3).⁴³ Table 2 lists detailed simulation parameters, which include

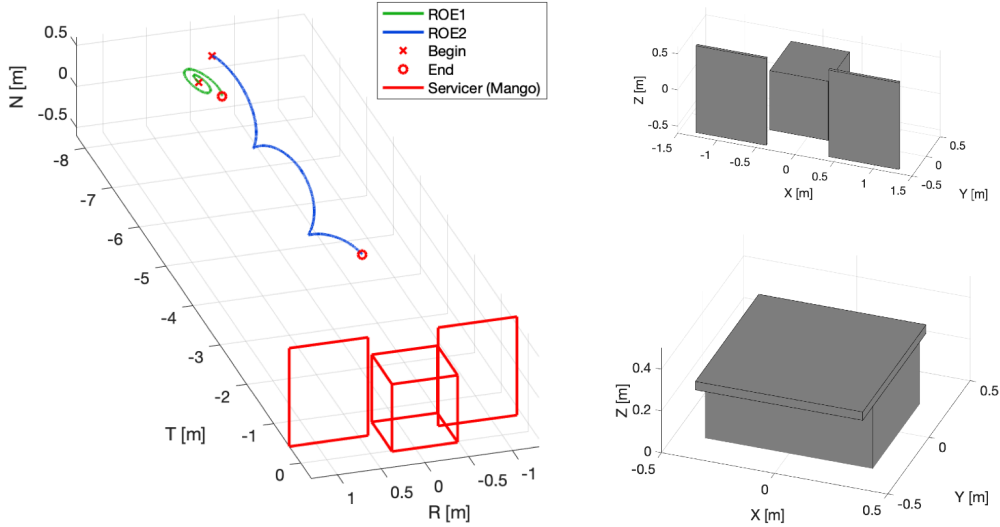


Figure 3: (Left) Relative trajectories of the target (Tango) with respect to the servicer (Mango). (Right) Simplified models of Mango (Top) and Tango (Bottom).

rigorous force and torque models for realistic ground-truth propagation. In order to evaluate these models, the servicer and target spacecraft are modeled as Mango and Tango from the PRISMA mission.⁹ The spacecraft parameters for force models are derived from D’Amico³⁵ and replicated in Table 3. It also lists the spacecraft parameters for evaluating the torque models. Specifically, in order to accurately propagate the attitude motion of both spacecraft, Mango and Tango are each modeled as an assembly of a cuboid and rectangular plates as visualized in Figure 3. The resulting relative trajectories of the target (Tango) with respect to the servicer (Mango) in RTN frame are also visualized in Figure 3. As expected from the initial ROE state, the target remains at about the same relative location with respect to the server in ROE1 throughout the simulation, whereas the servicer makes a spiral approach trajectory toward the target in ROE2.

Image Acquisition

Once the relative trajectories are simulated, two sets of images are created for respective rendezvous scenarios with the capture interval of 5 seconds. The first is `lightbox` images captured with the Testbed for Rendezvous and Optical Navigation (TRON) robotic testbed at the Space Rendezvous Laboratory (SLAB) of Stanford University. The facility consists of two KUKA 6 degrees-of-freedom robot arms holding a camera and a half-scale mockup model of the Tango spacecraft, respectively. The facility provides real-time pose of each robot’s end-effector with respect to the global reference frame within the testbed; therefore, the KUKA internal telemetry, along with the pose of infrared markers attached to both objects tracked by 12 Vicon Vero cameras,⁴⁴ can be jointly used to associate each image sample with high-accuracy pose labels. TRON also includes 10 lightboxes⁴⁵ which are calibrated to emulate the Earth albedo light in LEO. For more information on the facility, the readers are referred to Park et al.¹⁵

In order to simplify the data acquisition process, the target model’s position is fixed within the facility, and the camera is always directed along the length of the room. Given that the reference trajectories are in a dawn-dusk sun-synchronous orbit, only 4 lightboxes that are located in the cross-track direction are used to accurately emulate the effect of albedo light. Then, by fixing the mockup model’s position and calibrating the facility,⁴⁶ one can convert the relative pose to be simulated into the commands of the KUKA robot end-effectors. Each command is associated with a correct set of lightboxes and proper light intensities to accurately simulate the desired albedo effect. Once captured, the `lightbox` images are processed via the procedure identical to those in SPEED+.¹⁵

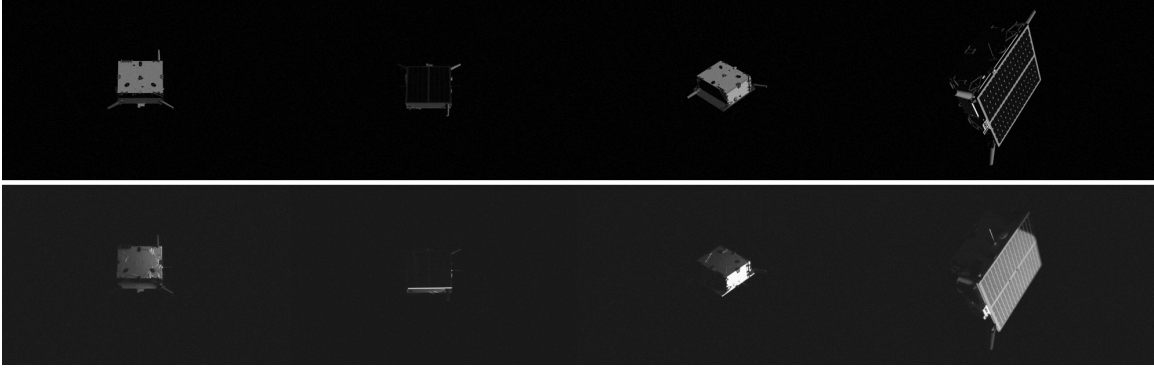


Figure 4: Samples of *synthetic* (*top*) and *lightbox* images (*bottom*) with identical pose labels.

The second set of images are *synthetic* images rendered with the OpenGL-based Optical Stimulator (OS)^{47,48} using the camera intrinsic parameters estimated from the calibration of TRON. Unlike SPEED+ *synthetic* images, the Earth images are not inserted in the background since the camera is always pointing in the along-track direction in the reference trajectories. The comparison of *synthetic* and *lightbox* images are presented in Figure 4, which shows that the images captured from TRON well emulate the illumination conditions present in their *synthetic* counterparts.

EXPERIMENTS

The proposed UKF with SPNv2 are tested on both *synthetic* and *lightbox* trajectories of SHIRT, but with more emphasis on the latter to examine the performance of the navigation filter across domain gap. Specifically, the performances of just SPNv2, UKF with constant process noise matrix $\mathbf{Q}_o = 1 \times 10^{-8} \mathbf{I}_{12 \times 12}$, and UKF with ASNC are evaluated. When ASNC is activated, the sliding window length is set to $N_W = 30$, which corresponds to 150 seconds window for 5 seconds measurement intervals. The filter state is initialized using the predictions of SPNv2 on the first image of the trajectory. Specifically, the relative angular velocity is computed based on the servicer’s absolute measurement (\mathbf{w}_S^S) and assuming the non-tumbling target (i.e., $\mathbf{w}_T^T = \mathbf{0}_{3 \times 1}$). The target’s relative velocity can be computed as $\mathbf{v}_{T/S} = \mathbf{w}_S^S \times \mathbf{r}_{T/S}$, where $\mathbf{r}_{T/S}$ is the target’s position predicted from SPNv2. Then, $(\mathbf{r}_{T/S}, \mathbf{v}_{T/S})$ are converted to $\delta\alpha$ using the servicer’s orbital state. The servicer’s absolute orbital and attitude states are assumed to be known perfectly unless noted otherwise. The filter’s performance is evaluated based on the translation error (E_T) and rotation error (E_R) defined in Eq. 1.

Results

First, Figure 5 shows the translation and rotation errors of the SPNv2 alone and UKF on the *lightbox* trajectories of SHIRT. It can be seen that when SPNv2 is used for pose predictions without any filter integration, the predicted poses are extremely noisy. In fact, the SPNv2 performs $E_T = 0.175\text{m}$ and $E_R = 17.167^\circ$ on ROE1 images and $E_T = 0.100\text{m}$ and $E_R = 4.669^\circ$ on ROE2 images on average. Note that the measurements are noisier for ROE1 since its images are much more challenging as the target is kept at a far distance (8m) and has much more restricted range of angle of view. However, when SPNv2 is integrated into the UKF with constant \mathbf{Q}_o , Figure 5 shows that the steady state errors are significantly reduced, and these are further improved when ASNC is implemented as the estimated orientation especially is smoothed out over the course of trajectories and kept below 5° . Moreover, ASNC enables much faster convergence of the filter by adaptively updating the process noise based on the underlying spacecraft dynamics. Overall, Figure 5 indicates that, given SPNv2 that is trained only on SPEED+ *synthetic* images, it is possible to quickly reach low steady-state errors on the *lightbox* trajectory images when combined into UKF with ASNC, even if the predictions of SPNv2 are noisy.

Next, the convergence behavior of a subset of the state vector is shown in Figures 6 and 7 for ROE1 and ROE2 *lightbox* trajectories, respectively. Specifically, the relative longitude ($\delta\lambda$) and the x -component of

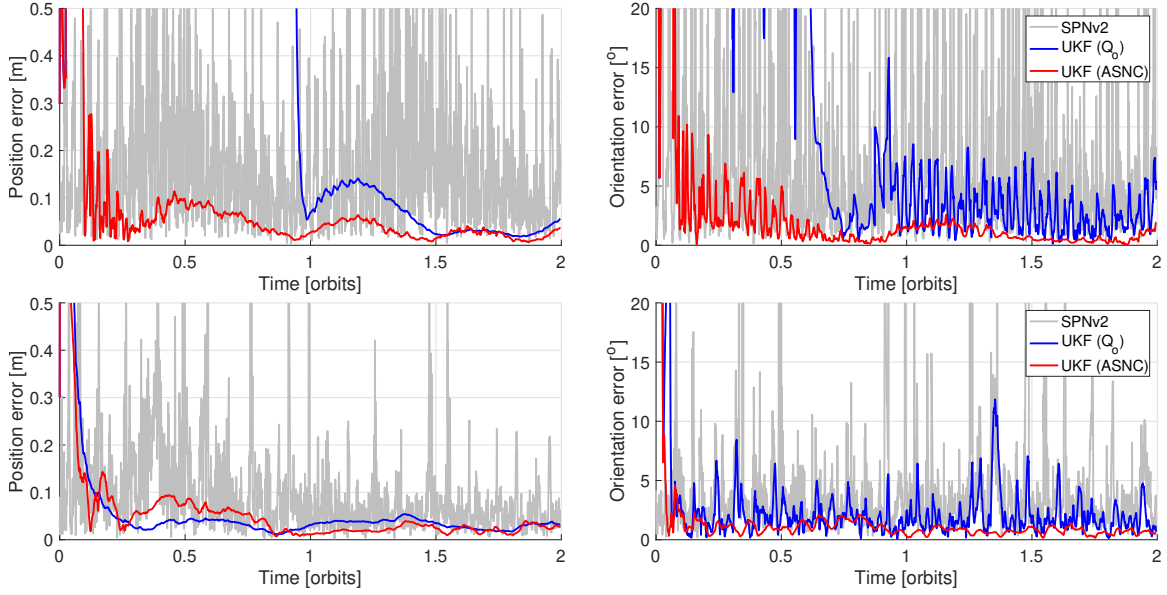


Figure 5: Position and orientation errors of SPNv2 and different UKF configurations on the lightbox trajectories of ROE1 (*top*) and ROE2 (*bottom*).

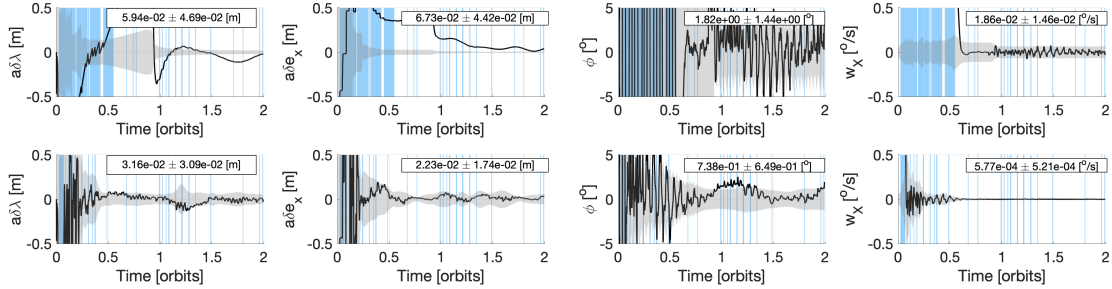


Figure 6: Convergence and the associated formal 3- σ bounds of the state vector elements on the ROE1 lightbox trajectory. UKF with constant Q_o (*top*) and ASNC (*bottom*) are considered. The boxed quantity denotes the mean error and standard deviation during the second orbit. The blue bars indicate all measurements are rejected at those time steps.

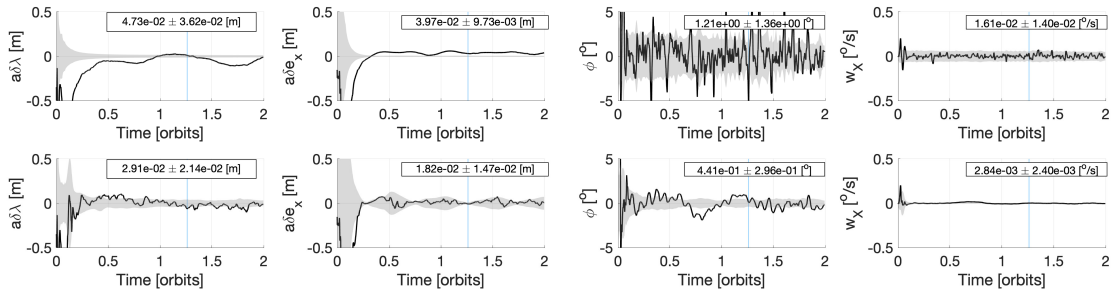


Figure 7: Convergence and the associated formal 3- σ bounds of the state vector elements on the ROE2 lightbox trajectory. UKF with constant Q_o (*top*) and ASNC (*bottom*) are considered. The boxed quantity denotes the mean error and standard deviation during the second orbit.

Table 4: Standard deviation of the noise injected to the servicer’s absolute state knowledge during MC simulations.

Element [unit]	σ
Position [m]	25
Velocity [m/s]	0.25
Orientation [°]	0.25
Angular Velocity [°/s]	6.075×10^{-4}

Table 5: Mean position and orientation errors of UKF with ASNC during the second orbit from 1000 MC simulations with imperfect absolute servicer state knowledge.

Trajectory	synthetic		lightbox	
	E_T [m]	E_R [°]	E_T [m]	E_R [°]
ROE1	0.089 ± 0.002	0.935 ± 0.014	0.073 ± 0.002	1.147 ± 0.136
ROE2	0.032 ± 0.001	0.559 ± 0.008	0.024 ± 0.004	0.776 ± 0.022

Table 6: Comparison of the UKF’s steady-state errors against the design requirements of the MDS of the Orbital Express vehicles.

Parameter [unit]	Design Req.	UKF (ROE1)	UKF (ROE2)
Axial capture distance [cm]	15	2.52 ± 1.61	1.98 ± 0.90
Lateral misalignment [cm]	5	1.27 ± 0.30	0.81 ± 0.45
Linear constant velocity [cm/s]	3	0.0034 ± 0.0022	0.0032 ± 0.0001
Angular capture misalignment (pitch/yaw) [°]	5	0.59 ± 0.27	0.58 ± 0.27
Angular capture misalignment (roll) [°]	5	0.24 ± 0.18	0.31 ± 0.20

the relative eccentricity vector (δe_x) scaled by the servicer’s semi-major axis, relative roll angle (ϕ), and the x -component of the relative angular velocity are evaluated. It is immediately obvious that ASNC accelerates the convergence of all elements especially on ROE1, in which UKF without ASNC cannot achieve convergence during the first orbit due to continuous measurement rejections based on the square Mahalanobis distance metric. Most importantly, when ASNC is activated, the $3\text{-}\sigma$ bounds associated with each state vector element better reflect the associated uncertainty induced by adverse illumination conditions and bad predictions due to domain gap.

The aforementioned results are obtained when the servicer’s absolute state knowledge is assumed to be perfect. Therefore, the robustness of UKF with ASNC is evaluated through 1000 Monte Carlo (MC) simulations in which random noises characterized in Table 4 are injected to the servicer’s absolute state at each time step. The results of MC simulations of UKF with ASNC on both *synthetic* and *lightbox* trajectories are found in Table 5 which shows the steady-state position and orientation errors during the second orbit. It shows that, despite imperfect absolute state knowledge of the servicer, the UKF with ASNC demonstrates consistent convergence behavior and accuracy on both *synthetic* and *lightbox* trajectories. It is noteworthy that for the steady-state position error, the estimated position is even better on the *lightbox* trajectories than on the *synthetic* ones, which is surprising considering the domain gap between these two image domains.

Finally, in order to assess the filter’s performance in terms of the typical pose accuracy requirements imposed during the rendezvous and docking processes, it is compared to the design requirements of the Mechanical Docking System (MDS) of the Orbital Express (OE) mission.⁴⁹ The comparison is justified by assuming that the steady-state error of the estimated relative pose during the close-proximity rendezvous would carry on to

the ensuing docking process. As shown in Table 6, the ROE state is converted to the relative cartesian position and velocity, and the former is broken into the error along the lateral and axial components. The orientation error is also converted into roll-pitch-yaw angles for comparison. Table 6 indicates that the relative orbital and attitude states estimated by UKF and SPNv2 during the v -bar hold (ROE1) and approach (ROE2) trajectories are far less than the docking requirements posed for the OE mission. Specifically, the lateral misalignment of the proposed UKF is on the centimeter-level which is much less than the 5cm requirement, and for all the other conditions, UKF achieves the steady-state error that is at least an order of magnitude smaller than the requirements of the OE mission despite using a single low SWaP-C monocular camera.

Overall, the experimental results demonstrate that the integration of SPNv2 into UKF and adaptive updates of the filter’s process noise covariance enable a remarkable performance of the neural network-based navigation filter in spaceborne close-proximity rendezvous scenarios. The performance is validated on both `synthetic` and `lightbox` trajectories of SHIRT, on the latter of which the SPNv2 alone would make noisy measurements due to domain gap.

CONCLUSION

This paper has presented the integration of the Spacecraft Pose Network v2 (SPNv2), a convolutional neural network for vision-based spacecraft pose estimation across domain gap, into an Unscented Kalman Filter (UKF) to enable robust and accurate tracking of the position and orientation of a known, noncooperative target spacecraft in close-proximity rendezvous scenarios. In order to improve the convergence and accuracy of the filter across domain gap, the process noise covariance matrices for the orbital and attitude states are adaptively updated at each time step via adaptive state noise compensation. The paper also introduces the Satellite Hardware-In-the-loop Rendezvous Trajectories (SHIRT) dataset, which consists of `synthetic` and `lightbox` images of two close-range rendezvous trajectories simulated with SLAB’s Satellite Software (S^3). As the `synthetic` and `lightbox` images have very different visual characteristics of the same spacecraft in an identical trajectory, SHIRT enables a comprehensive side-by-side comparison of a navigation filter’s performance across domain gap. The proposed UKF, which uses the SPNv2 trained on synthetic images as an image processor, is shown to reach sub-decimeter-level position and degree-level orientation errors at steady-state on both domains of trajectory images, successfully bridging the domain gap present in the dataset.

In the future, SHIRT will be extended to include the trajectories and images of the docking scenarios, which is another pivotal component of the techniques required for safe and autonomous servicing missions. Moreover, while the computational efficiency of SPNv2 during pose inference is not considered in this paper, a future work must investigate on how to improve the architecture and training procedure of SPNv2 to render it smaller and more computationally efficient while maintaining the same level of performance across domain gap. The proposed UKF design and ASNC will also be further stress-tested on trajectories with varying spin rate of the target to evaluate its robustness on the target’s tumbling rate. Finally, both SPNv2 and the navigation filter will be extended to an unknown target spacecraft.

ACKNOWLEDGEMENT

This work is supported by the Air Force Office of Scientific Research (AFOSR) via Centauri under the project titled Modular State-Adaptive Landmark Tracking. The authors would like to thank OHB Sweden for the 3D model of the Tango spacecraft used to create the images used in this article. The authors also thank Nathan Stacey at Stanford’s Space Rendezvous Laboratory for helpful discussions.

APPENDIX: PROCESS NOISE COVARIANCE MODELS

ROE State

For $\delta\alpha' = \alpha_T - \alpha_S$, where α is a vector of equinoctial elements, the linear mapping matrix $\mathbf{X}'_{k,i}$ for $i \in \{r, t, n\}$ is given as²⁷

$$\mathbf{X}'_k{}^r = \Delta t_k \mathbf{\Gamma}_k^r \mathbf{\Gamma}_k^{r\top} + \frac{3n\Delta t_k^2}{4a} \begin{bmatrix} \mathbf{0}_{5 \times 5} & \mathbf{S}_r \\ \mathbf{S}_r^\top & \frac{n}{a} \bar{A}^2 \Delta t_k - 2\bar{A}\bar{K} \end{bmatrix}, \quad (40)$$

$$\mathbf{X}'_k{}^t = \Delta t_k \mathbf{\Gamma}_k^t \mathbf{\Gamma}_k^{t\top} + \frac{3n\Delta t_k^2}{4a} \begin{bmatrix} \mathbf{0}_{5 \times 5} & \mathbf{S}_t \\ \mathbf{S}_t^\top & \frac{n}{a} \bar{B}^2 \Delta t_k - 2\bar{B}\bar{L} \end{bmatrix}, \quad (41)$$

$$\mathbf{X}'_k{}^n = \Delta t_k \mathbf{\Gamma}_k^n \mathbf{\Gamma}_k^{n\top}. \quad (42)$$

Here, $\mathbf{\Gamma}_k = [\mathbf{\Gamma}_k^r \ \mathbf{\Gamma}_k^t \ \mathbf{\Gamma}_k^n] \in \mathbb{R}^{6 \times 3}$ denotes the time derivative of the equinoctial elements given by the Gauss Variational Equations,

$$\mathbf{\Gamma}_k = \begin{bmatrix} \bar{A} & \bar{B} & 0 \\ \bar{C} & \bar{D} & \bar{E} \\ \bar{F} & \bar{G} & \bar{H} \\ 0 & 0 & \bar{I} \\ 0 & 0 & \bar{J} \\ \bar{K} & \bar{L} & \bar{M} \end{bmatrix}, \quad (43)$$

where the elements of $\mathbf{\Gamma}_k$ are based on the servier's orbital state at t_k , and $\mathbf{S}_r = -[\bar{A}^2 \ \bar{A}\bar{C} \ \bar{A}\bar{F} \ 0 \ 0]^\top$, $\mathbf{S}_t = -[\bar{B}^2 \ \bar{B}\bar{D} \ \bar{B}\bar{G} \ 0 \ 0]^\top$. The barred elements are available in Stacey and D'Amico²⁷ and are not reproduced here for brevity.

Attitude State

The sub-matrices of Eq. 39 are given as

$$\begin{aligned} \bar{\mathbf{A}}_i &= \int_{t_{k-1}}^{t_k} \mathbf{\Lambda}_{1,i}(t_k - \tau) \mathbf{\Lambda}_{1,i}(t_k - \tau)^\top d\tau = \frac{\Delta t_k^3}{3} \mathbf{e}_i \mathbf{e}_i^\top + \zeta_{c_1 c_1} \mathbf{W}_{1,i} \mathbf{W}_{1,i}^\top + \zeta_{s_1 s_1} \mathbf{V}_{1,i} \mathbf{V}_{1,i}^\top \\ &\quad + \zeta_{t c_1} (\mathbf{e}_i \mathbf{W}_{1,i}^\top + \mathbf{W}_{1,i} \mathbf{e}_i^\top) + \zeta_{t s_1} (\mathbf{e}_i \mathbf{V}_{1,i}^\top + \mathbf{V}_{1,i} \mathbf{e}_i^\top) + \zeta_{c_1 s_1} (\mathbf{W}_{1,i} \mathbf{V}_{1,i}^\top + \mathbf{V}_{1,i} \mathbf{W}_{1,i}^\top), \end{aligned} \quad (44)$$

$$\begin{aligned} \bar{\mathbf{B}}_i &= \int_{t_{k-1}}^{t_k} \mathbf{\Lambda}_{1,i}(t_k - \tau) \mathbf{\Lambda}_{2,i}(t_k - \tau)^\top d\tau = \frac{\Delta t_k^2}{2} \mathbf{e}_i \mathbf{e}_i^\top + \zeta_{t s_2} \mathbf{e}_i \mathbf{W}_{2,i}^\top + \zeta_{t c_2} \mathbf{e}_i \mathbf{V}_{2,i}^\top + \zeta_{c_1} \mathbf{W}_{1,i} \mathbf{e}_i^\top \\ &\quad + \zeta_{c_1 s_2} \mathbf{W}_{1,i} \mathbf{W}_{2,i}^\top + \zeta_{c_1 c_2} \mathbf{W}_{1,i} \mathbf{V}_{2,i}^\top + \zeta_{s_1} \mathbf{V}_{1,i} \mathbf{e}_i^\top + \zeta_{s_1 s_2} \mathbf{V}_{1,i} \mathbf{W}_{2,i}^\top + \zeta_{s_1 c_2} \mathbf{V}_{1,i} \mathbf{V}_{2,i}^\top, \end{aligned} \quad (45)$$

$$\begin{aligned} \bar{\mathbf{C}}_i &= \int_{t_{k-1}}^{t_k} \mathbf{\Lambda}_{2,i}(t_k - \tau) \mathbf{\Lambda}_{2,i}(t_k - \tau)^\top d\tau = \Delta t_k \mathbf{e}_i \mathbf{e}_i^\top + \zeta_{c_2 c_2} \mathbf{V}_{2,i} \mathbf{V}_{2,i}^\top + \zeta_{s_2 s_2} \mathbf{W}_{2,i} \mathbf{W}_{2,i}^\top \\ &\quad + \zeta_{c_2} (\mathbf{e}_i \mathbf{V}_{2,i}^\top + \mathbf{V}_{2,i} \mathbf{e}_i^\top) + \zeta_{s_2} (\mathbf{e}_i \mathbf{W}_{2,i}^\top + \mathbf{W}_{2,i} \mathbf{e}_i^\top) + \zeta_{c_2 s_2} (\mathbf{W}_{2,i} \mathbf{V}_{2,i}^\top + \mathbf{V}_{2,i} \mathbf{W}_{2,i}^\top), \end{aligned} \quad (46)$$

where $\mathbf{W}_j = [\hat{\mathbf{w}}_j]_\times = [\mathbf{W}_{j,x} \ \mathbf{W}_{j,y} \ \mathbf{W}_{j,z}]$, $\mathbf{V}_j = [\hat{\mathbf{w}}_j]_\times^2 = [\mathbf{V}_{j,x} \ \mathbf{V}_{j,y} \ \mathbf{V}_{j,z}]$. Recall that \mathbf{w}_1 denotes $\mathbf{w}_{S/T,k}^T$, and \mathbf{w}_2 denotes $\mathbf{w}_{T,k}^T$. The ζ coefficients are then expressed analytically by evaluating the integrals of each term. Defining $c_1 = \cos \frac{w_1 \Delta t_k}{2}$, $s_1 = \sin \frac{w_1 \Delta t_k}{2}$, $c_2 = \cos w_2 \Delta t_k$, $s_2 = \sin w_2 \Delta t_k$, the coefficients are given

as

$$\begin{aligned}
\zeta_{c_1} &= \int_{t_{k-1}}^{t_k} \frac{2}{w_1} \left[1 - \cos \left(\frac{w_1}{2} (t_k - \tau) \right) \right] d\tau = \frac{2}{w_1} \left(\Delta t_k - \frac{2}{w_1} s_1 \right) \\
\zeta_{s_1} &= \int_{t_{k-1}}^{t_k} \left(t_k - \tau \right) - \frac{2}{w_1} \sin \left(\frac{w_1}{2} (t_k - \tau) \right) d\tau = \frac{\Delta t_k^2}{2} + \frac{4}{w_1^2} (c_1 - 1) \\
\zeta_{t c_1} &= \int_{t_{k-1}}^{t_k} \frac{2}{w_1} (t_k - \tau) \left[1 - \cos \left(\frac{w_1}{2} (t_k - \tau) \right) \right] d\tau = \frac{2}{w_1} \left[\frac{\Delta t_k^2}{2} - \frac{2}{w_1} \Delta t_k s_1 - \frac{4}{w_1^2} (c_1 - 1) \right] \\
\zeta_{t s_1} &= \int_{t_{k-1}}^{t_k} (t_k - \tau) \left[(t_k - \tau) - \frac{2}{w_1} \sin \left(\frac{w_1}{2} (t_k - \tau) \right) \right] d\tau = \frac{\Delta t_k^3}{3} + \frac{4}{w_1^2} \left(\Delta t_k c_1 - \frac{2}{w_1} s_1 \right) \\
\zeta_{c_1 c_1} &= \int_{t_{k-1}}^{t_k} \frac{4}{w_1^2} \left[1 - \cos \left(\frac{w_1}{2} (t_k - \tau) \right) \right]^2 d\tau = \frac{4}{w_1^2} \left(\frac{3}{2} \Delta t_k - \frac{4}{w_1} s_1 + \frac{1}{w_1} s_1 c_1 \right) \\
\zeta_{s_1 s_1} &= \int_{t_{k-1}}^{t_k} \left[(t_k - \tau) - \frac{2}{w_1} \sin \left(\frac{w_1}{2} (t_k - \tau) \right) \right]^2 d\tau = \frac{\Delta t_k^3}{3} + \frac{4}{w_1^2} \left(2 \Delta t_k c_1 - \frac{4}{w_1} s_1 + \frac{\Delta t_k}{2} - \frac{1}{w_1} s_1 c_1 \right) \\
\zeta_{c_1 s_1} &= \int_{t_{k-1}}^{t_k} \frac{2}{w_1} \left[1 - \cos \left(\frac{w_1}{2} (t_k - \tau) \right) \right] \left[(t_k - \tau) - \frac{2}{w_1} \sin \left(\frac{w_1}{2} (t_k - \tau) \right) \right] d\tau = \frac{1}{w_1} \left(\Delta t_k - \frac{2}{w_1} s_1 \right)^2 \\
\zeta_{c_2} &= \int_{t_{k-1}}^{t_k} (1 - \cos w_2 (t_k - \tau)) d\tau = \Delta t_k - \frac{1}{w_2} s_2 \\
\zeta_{s_2} &= \int_{t_{k-1}}^{t_k} -\sin w_2 (t_k - \tau) d\tau = \frac{1}{w_2} (c_2 - 1) \\
\zeta_{t c_2} &= \int_{t_{k-1}}^{t_k} (t_k - \tau) (1 - \cos w_2 (t_k - \tau)) d\tau = \frac{\Delta t_k^2}{2} + \frac{1}{w_2^2} (1 - c_2 - w_2 \Delta t_k s_2) \\
\zeta_{t s_2} &= \int_{t_{k-1}}^{t_k} -(t_k - \tau) \sin w_2 (t_k - \tau) d\tau = \frac{\Delta t_k}{w_2} c_2 - \frac{1}{w_2^2} s_2 \\
\zeta_{c_2 c_2} &= \int_{t_{k-1}}^{t_k} (1 - \cos w_2 (t_k - \tau))^2 d\tau = 1.5 \Delta t_k + \frac{s_2}{w_2} \left(\frac{1}{2} c_2 - 2 \right) \\
\zeta_{s_2 s_2} &= \int_{t_{k-1}}^{t_k} \sin^2 w_2 (t_k - \tau) d\tau = \frac{1}{2} \left(\Delta t_k - \frac{1}{w_2} s_2 c_2 \right) \\
\zeta_{c_2 s_2} &= \int_{t_{k-1}}^{t_k} -(1 - \cos w_2 (t_k - \tau)) \sin w_2 (t_k - \tau) d\tau = -\frac{1}{2w_2} (1 - c_2)^2 \\
\zeta_{c_1 c_2} &= \int_{t_{k-1}}^{t_k} \frac{2}{w_1} \left[1 - \cos \left(\frac{w_1}{2} (t_k - \tau) \right) \right] (1 - \cos w_2 (t_k - \tau)) d\tau = \\
&\quad \frac{2}{w_1} \left(\zeta_{c_2} - \frac{2}{w_1} s_1 + \frac{s_1 c_2 - c_1 s_2}{w_1 - 2w_2} + \frac{s_1 c_2 + c_1 s_2}{w_1 + 2w_2} \right) \\
\zeta_{c_1 s_2} &= \int_{t_{k-1}}^{t_k} \frac{2}{w_1} \left[1 - \cos \left(\frac{w_1}{2} (t_k - \tau) \right) \right] (-\sin w_2 (t_k - \tau)) d\tau = \\
&\quad \frac{2}{w_1} \left(\zeta_{s_2} + \frac{1 - c_1 c_2 + s_1 s_2}{w_1 + 2w_2} - \frac{1 - c_1 c_2 - s_1 s_2}{w_1 - 2w_2} \right) \\
\zeta_{s_1 c_2} &= \int_{t_{k-1}}^{t_k} \left[(t_k - \tau) - \frac{2}{w_1} \sin \left(\frac{w_1}{2} (t_k - \tau) \right) \right] (1 - \cos w_2 (t_k - \tau)) d\tau = \\
&\quad \zeta_{t c_2} - \frac{4}{w_1^2} (1 - c_1) + \frac{2}{w_1} \left(\frac{1 - c_1 c_2 + s_1 s_2}{w_1 + 2w_2} + \frac{1 - c_1 c_2 - s_1 s_2}{w_1 - 2w_2} \right) \\
\zeta_{s_1 s_2} &= \int_{t_{k-1}}^{t_k} \left[(t_k - \tau) - \frac{2}{w_1} \sin \left(\frac{w_1}{2} (t_k - \tau) \right) \right] (-\sin w_2 (t_k - \tau)) d\tau = \\
&\quad \zeta_{t s_2} + \frac{2}{w_1} \left(\frac{s_1 c_2 - c_1 s_2}{w_1 - 2w_2} - \frac{s_1 c_2 + c_1 s_2}{w_1 + 2w_2} \right)
\end{aligned}$$

REFERENCES

- [1] B. B. Reed, R. C. Smith, B. J. Naasz, J. F. Pellegrino, and C. E. Bacon, "The Restore-L servicing mission," *Aiaa Space 2016*, 2016.
- [2] J. L. Forshaw, G. S. Aglietti, N. Navarathinam, H. Kadhem, T. Salmon, A. Pisseloup, E. Joffre, T. Chabot, I. Retat, R. Axthelm, and et al., "RemoveDEBRIS: An in-orbit active debris removal demonstration mission," *Acta Astronautica*, vol. 127, p. 448–463, 2016.
- [3] S. Sharma and S. D'Amico, "Pose estimation for non-cooperative spacecraft rendezvous using neural networks," in *2019 AAS/AIAA Space Flight Mechanics Meeting, Ka'anapali, Maui, HI*, January 13-17 2019.
- [4] T. H. Park, S. Sharma, and S. D'Amico, "Towards robust learning-based pose estimation of noncooperative spacecraft," in *2019 AAS/AIAA Astrodynamics Specialist Conference, Portland, Maine*, August 11-15 2019.
- [5] L. P. Cassinis, R. Fonod, E. Gill, I. Ahrns, and J. G. Fernandez, "Cnn-based pose estimation system for close-proximity operations around uncooperative spacecraft," in *AIAA Scitech 2020 Forum*, 2020.
- [6] K. Black, S. Shankar, D. Fonseca, J. Deutsch, A. Dhira, and M. Akella, "Real-time, flight-ready, non-cooperative spacecraft pose estimation using monocular imagery," in *31st AAS/AIAA Space Flight Mechanics Meeting*, February 2021.
- [7] B. Chen, J. Cao, Á. P. Bustos, and T.-J. Chin, "Satellite pose estimation with deep landmark regression and nonlinear pose refinement," *2019 IEEE/CVF International Conference on Computer Vision Workshop (ICCVW)*, pp. 2816–2824, 2019.
- [8] P. F. Proenca and Y. Gao, "Deep learning for spacecraft pose estimation from photorealistic rendering," *arXiv preprint arXiv:1907.04298*, 2019.
- [9] S. D'Amico, P. Bodin, M. Delpech, and R. Noteborn, "PRISMA," in *Distributed Space Missions for Earth System Monitoring Space Technology Library* (M. D'Errico, ed.), vol. 31, ch. 21, pp. 599–637, 2013.
- [10] M. Kisantal, S. Sharma, T. H. Park, D. Izzo, M. Märtens, and S. D'Amico, "Satellite pose estimation challenge: Dataset, competition design and results," *IEEE Transactions on Aerospace and Electronic Systems*, vol. 56, no. 5, pp. 4083–4098, 2020.
- [11] S. Sharma, T. H. Park, and S. D'Amico, "Spacecraft pose estimation dataset (speed)." Stanford Digital Repository. Available at: <https://doi.org/10.25740/dz692fn7184>, 2019.
- [12] L. Pasqualetto Cassinis, A. Menicucci, E. Gill, I. Ahrns, and J. Gil Fernandez, "On-ground validation of a cnn-based monocular pose estimation system for uncooperative spacecraft," in *8th European Conference on Space Debris*, vol. 8, 2021.
- [13] S. Ben-David, J. Blitzer, K. Crammer, and F. Pereira, "Analysis of representations for domain adaptation," in *Advances in Neural Information Processing Systems*, 2007.
- [14] X. Peng, B. Usman, N. Kaushik, J. Hoffman, D. Wang, and K. Saenko, "VisDA: The visual domain adaptation challenge," 2017.
- [15] T. H. Park, M. Märtens, G. Lecuyer, D. Izzo, and S. D'Amico, "SPEED+: Next-generation dataset for spacecraft pose estimation across domain gap," *arXiv preprint arXiv:2110.03101*, 2021.
- [16] T. H. Park, M. Märtens, G. Lecuyer, D. Izzo, and S. D'Amico, "Next generation spacecraft pose estimation dataset (SPEED+)." Stanford Digital Repository, 2021. Available at <https://purl.stanford.edu/wv398fc4383>.
- [17] T. H. Park and S. D'Amico, "Robust multi-task learning and online refinement for spacecraft pose estimation across domain gap," *arXiv preprint arXiv:2203.04275*, 2022.
- [18] P. T. Jackson, A. Atapour-Abarghouei, S. Bonner, T. P. Breckon, and B. Obara, "Style augmentation: Data augmentation via style randomization," in *Proceedings of the IEEE Conference on Computer Vision and Pattern Recognition Workshops*, pp. 83–92, 2019.
- [19] S. Ioffe and C. Szegedy, "Batch normalization: Accelerating deep network training by reducing internal covariate shift," in *Proceedings of the 32nd International Conference on Machine Learning*, 2015.
- [20] S. J. Julier and J. K. Uhlmann, "Unscented filtering and nonlinear estimation," *Proceedings of the IEEE*, vol. 92, no. 3, pp. 401–422, 2004.
- [21] B. E. Tweddle and A. Saenz-Otero, "Relative computer vision-based navigation for small inspection spacecraft," *Journal of Guidance, Control, and Dynamics*, vol. 38, no. 5, pp. 969–978, 2015.
- [22] S. Sharma and S. D'Amico, "Reduced-dynamics pose estimation for non-cooperative spacecraft rendezvous using monocular vision," in *40th Annual AAS Guidance and Control Conference, Breckenridge, Colorado*, February 2-8 2017.
- [23] J. L. Crassidis and F. L. Markley, "Unscented filtering for spacecraft attitude estimation," *Journal of Guidance, Control, and Dynamics*, vol. 26, no. 4, pp. 536–542, 2003.
- [24] H. Schaub and J. Junkins, "Stereographic orientation parameters for attitude dynamics: A generalization of the Rodrigues parameters," *Journal of the Astronautical Sciences*, vol. 44, 01 1995.
- [25] N. Stacey and S. D'Amico, "Adaptive and dynamically constrained process noise estimation for orbit determination," *IEEE Transactions on Aerospace and Electronic Systems*, vol. 57, no. 5, pp. 2920–2937, 2021.

- [26] K. Myers and B. Tapley, "Adaptive sequential estimation with unknown noise statistics," *IEEE Transactions on Automatic Control*, vol. 21, no. 4, pp. 520–523, 1976.
- [27] N. Stacey and S. D'Amico, "Analytical process noise covariance modeling for absolute and relative orbits," *Acta Astronautica*, vol. 194, pp. 34–47, 2022.
- [28] Y. Bukschat and M. Vetter, "Efficientpose: An efficient, accurate and scalable end-to-end 6d multi object pose estimation approach," 2020.
- [29] S. Sharma and S. D'Amico, "Comparative assessment of techniques for initial pose estimation using monocular vision," vol. 123, pp. 435–445, 2016.
- [30] V. Lepetit, F. Moreno-Noguer, and P. Fua, "EPnP: An accurate $O(n)$ solution to the PnP problem," *International Journal of Computer Vision*, vol. 81, no. 2, p. 155–166, 2008.
- [31] Y. Wu and K. He, "Group normalization," in *Proceedings of the European Conference on Computer Vision (ECCV)*, September 2018.
- [32] C. Beierle, A. Norton, B. Macintosh, and S. D'Amico, "Two-stage attitude control for direct imaging of exoplanets with a CubeSat telescope," in *Space Telescopes and Instrumentation 2018: Optical, Infrared, and Millimeter Wave*, vol. 10698, pp. 630 – 644, International Society for Optics and Photonics, SPIE, 2018.
- [33] A. W. Koenig, T. Guffanti, and S. D'Amico, "New state transition matrices for spacecraft relative motion in perturbed orbits," *Journal of Guidance, Control, and Dynamics*, vol. 40, no. 7, pp. 1749–1768, 2017.
- [34] V. Capuano, K. Kim, J. Hu, A. Harvard, and S.-J. Chung, "Monocular-based pose determination of uncooperative known and unknown space objects," in *69th International Astronautical Congress (IAC), Bremen, Germany*, 1-5 October 2018.
- [35] S. D'Amico, *Autonomous formation flying in low earth orbit*. PhD thesis, Technical University of Delft, 2010.
- [36] S. D'Amico, M. Benn, and J. L. Jørgensen, "Pose estimation of an uncooperative spacecraft from actual space imagery," *International Journal of Space Science and Engineering*, vol. 2, no. 2, p. 171, 2014.
- [37] J. Dormand and P. Prince, "A family of embedded runge-kutta formulae," *Journal of Computational and Applied Mathematics*, vol. 6, no. 1, pp. 19–26, 1980.
- [38] J. C. Ries, S. V. Bettadpur, R. J. Eanes, Z. Kang, U.-D. Ko, C. M. McCullough, P. Nagel, N. Pie, S. R. Poole, T. Richter, H. Save, and B. D. Tapley, "The development and evaluation of the global gravity model GGM05," *CSR-16-02, Center for Space Research, The University of Texas at Austin*, 2016.
- [39] J. M. Picone, A. E. Hedin, D. P. Drob, and A. C. Aikin, "NRLMSISE-00 empirical model of the atmosphere: Statistical comparisons and scientific issues," *Journal of Geophysical Research: Space Physics*, vol. 107, no. A12, pp. SIA 15–1–SIA 15–16, 2002.
- [40] E. K. A. Gill and O. Montenbruck, *Satellite orbits: Models, methods and applications*. Springer, 2013.
- [41] C. S. Corporation, and J. R. Wertz, *Spacecraft attitude determination and control / edited by James R. Wertz ; written by members of the technical staff Attitude Systems Operation, Computer Sciences Corporation*. Reidel Dordrecht ; Boston, 1978.
- [42] P. Alken, T. Erwan, C. Beggan, H. Amit, J. Aubert, J. Baerenzung, T. Bondar, W. Brown, S. Califf, A. Chambout, A. Chulliat, G. Cox, C. Finlay, A. Fournier, N. Gillet, A. Grayver, M. Hammer, M. Holschneider, L. Huder, and B. Zhou, "International geomagnetic reference field: the thirteenth generation," *Earth, Planets and Space*, vol. 73, 07 2020.
- [43] V. Giraldo and S. D'Amico, "Development of the stanford gnss navigation testbed for distributed space systems," in *Institute of Navigation, International Technical Meeting, Reston, Virginia*, January 29 - February 1 2018.
- [44] "Vero: Compact super wide camera by vicon." <https://www.vicon.com/hardware/cameras/vero/>. Accessed April 29, 2021.
- [45] "Verification of light-box devices for earth albedo simulation." Technical Note, Stanford Space Rendezvous Lab (SLAB), January (2016).
- [46] T. H. Park, J. Bosse, and S. D'Amico, "Robotic testbed for rendezvous and optical navigation: Multi-source calibration and machine learning use cases," in *2021 AAS/AIAA Astrodynamics Specialist Conference, Big Sky, Virtual*, August 9-11 2021.
- [47] S. Sharma, C. Beierle, and S. D'Amico, "Pose estimation for non-cooperative spacecraft rendezvous using convolutional neural networks," in *2018 IEEE Aerospace Conference*, pp. 1–12, March 2018.
- [48] C. Beierle and S. D'Amico, "Variable-magnification optical stimulator for training and validation of spaceborne vision-based navigation," *Journal of Spacecraft and Rockets*, vol. 56, pp. 1–13, Feb 2019.
- [49] S. S. Christiansen and T. Nilson, "Docking system mechanism utilized on orbital express program," 2008.